

PAPER • OPEN ACCESS

Capability of active thermography to detect and localize pores in Metal Additive Manufacturing materials

To cite this article: Ester D'Accardi *et al* 2021 *IOP Conf. Ser.: Mater. Sci. Eng.* **1038** 012018

View the [article online](#) for updates and enhancements.



240th ECS Meeting ORLANDO, FL

Orange County Convention Center Oct 10-14, 2021



Abstract submission due: April 9

SUBMIT NOW

Capability of active thermography to detect and localize pores in Metal Additive Manufacturing materials

Ester D'Accardi¹, Alexander Ulbricht², Rainer Krankenhagen², Davide Palumbo¹, Umberto Galietti¹

¹ Politecnico di Bari - Dipartimento di Meccanica, Matematica e Management, Via Orabona 4, 70125 Bari, Italy

² Bundesanstalt für Materialforschung und -prüfung (BAM), Unter den Eichen 87, 12205 Berlin, Germany

E-mail: ester.daccardi@poliba.it

Abstract. Active thermography is a fast, contactless and non-destructive technique that can be used to detect internal defects in different types of material. Volumetric irregularities such as the presence of pores in materials produced by the Additive Manufacturing processes can strongly affect the thermophysical and the mechanical properties of the final component.

In this work, an experimental investigation aimed at detecting different pores in a sample made of stainless AISI 316L produced by Laser Powder Bed Fusion (L-PBF) was carried out using pulsed thermography in reflection mode. The capability of the technique and the adopted setups in terms of geometrical and thermal resolution, acquisition frequency and energy density of the heating source were assessed to discern two contiguous pores as well as to detect a single pore. Moreover, a quantitative indication about the minimum resolvable pore size among the available and analysed defects was provided. A powerful tool to assess the limits and the opportunities of the pulsed technique in terms of detectability and localizability was provided by comparing active thermography results to Computed Tomography as well as a related Finite Element Analysis (FEA) to simulate the pulsed heating transfer with Comsol.

1. Introduction

One of the most advanced technologies of Metal Additive Manufacturing (AM) is the Laser Powder Bed Fusion process (L-PBF), also known as Selective Laser Melting (SLM) [1]-[2]. This process involves the deposition and fusion, layer by layer, of very fine metal powders; the structure and the quality of the final component strongly depends on several processing parameters, such as laser power, laser scanning path, and scan speed. The variables that influence the process are usually categorized into controllable ones (possible to modify), such as laser power and scan speed, or as predefined (set at the beginning of each build) material properties, such as powder size and distribution [3].

A large number of controllable and predefined process parameters as summarized by Mani et al. [4] have a complex influence over the transient thermal behaviour of the melt pool, often resulting in unexpected presence of different defects, such as pores, high surface roughness, thermal cracking, and delamination. In particular, pores are typical and spread defects in AM. The formation mechanism can be summarized as follows: when some AM processes are operated at very high-power density, by typically decreasing the laser scan speed somewhere, deposition or melting may be performed in keyhole mode [5]. Without careful control of keyhole mode melting, keyholes can become unstable



and repeatedly form and collapse, causing voids inside the deposit that consists of entrapped vapor. The size of keyhole porosity can vary depending on the shape and size of the keyhole [5]-[8].

There are several destructive and non-destructive techniques available to have a measure of these spread micropores.

The Archimedes' method [9] is the simplest method for measuring the overall porosity of an AM component. The volume percentage of porosity is estimated by starting from the density of the component. However, the shape, size, and distribution of the pores cannot be determined using this method. Besides, if pores are filled with powder, Archimedes' method also underestimates their correct volume. Therefore, this is not the best method for L-PBF components.

Optical Microscopy [10] is a widely used destructive method to measure porosity; again, the volume of the pores cannot be accurately measured using this technique. Also, another problem is that this method is not suitable for measuring very small pores.

Lab X-ray Micro Computed Tomography (μ CT) is a non-destructive method to quantitatively analyse the 3D shape and size of internal structures of AM components. The achievable resolution is mainly limited by the size of the sample and the size of the focal spot of the used X-ray tube. In literature μ CT had been applied to analyse voids in metallic AM parts achieving a resolution down to a few micrometres [5], [8]-[13].

In general, as already demonstrated in different works [9]-[13], both Scanning Electron Microscope (SEM) and μ CT can accurately measure the shape, size, and distribution of very small pores (in particular, SEM works in the nm range and CT in the μ m one); however, these methods are time-consuming and require high-cost instrumentations.

Alternatively, passive and active thermography techniques can be used to analyse samples non-destructively. Thermographic techniques could represent an efficient tool both for the on-site control (passive thermography, temperature monitoring) and off-line (active thermography, pulsed and lock-in) due to their versatility, costs and time required for testing and analysis, which are remarkably competitive with other methods of NDT [14]-[16].

The active thermography uses external heat sources for heating the object to be inspected in order to establish the necessary heat flow capable of generating differences of temperature into the specimen. In the last years, active thermography techniques were used in many applications regarding both metals and composites, and for detecting a wide defects variety such as delaminations, cracks and pores [17]-[22]. In the literature, systematic porosity investigations with active thermography have only been performed in Carbon Fiber Reinforced Plastics (CFRP) structures [23]-[24] or during welding of aluminium alloy [25]-[26]. However, more studies are required concerning the quantitative assessment of pores in metals [27], especially for very widespread additive products. Indeed, AM components present intrinsic peculiarities such as a high surface roughness and complex geometry that make them difficult to investigate with traditional NDT techniques.

In this work, we studied the possibility of diagnosing and localizing the presence of pores in components of AISI 316 L steel produced by the L-PBF process. In particular, the process parameters were changed during the AM process to introduce artificial defects within a specimen with a rectangular cross-section. Results from μ CT analysis showed the presence of a network of voids that can be considered as micro-structured defects, with complex shape.

The Pulsed Thermography technique was performed using a diode laser system (942 nm) for exciting the specimen and a cooled IR detector for acquiring thermal sequences. Numerical and experimental PT tests were carried out for investigating the emissivity issue of the material and the effect of using a high emissivity coating on the specimen with the aim to detect and characterize the inner defects. It was observed that the presence of a black graphite coating allows of increasing the absorbed energy and make the emissivity of the surface uniform. In this regard, the coating influences the thermal contrast and then the capability of technique of detecting volumetric defects. On the contrary, inhomogeneities of the coating could impair the spatial resolution.

The adopted approach would provide a powerful tool (both FEM and experimental investigations) to have an indication for the application of the pulsed thermographic technique to materials produced

by the AM process, and more in general, it focuses on the parameters of the tests that mainly influence the capability of detecting single or contiguous pores.

2. Material, methods and experimental set-ups

2.1. Inspected material, process parameters and defects geometry

Several specimens made of AISI 316L steel (example depicted in figure 1) were produced by means of the L-PBF technique, varying the process parameters. In figure 1 is shown the surface of the specimen investigated in this work in its state after the AM process, together with the same surface after depositing a graphite coating.



Figure 1. Surface conditions of the analysed specimen with a high roughness, typical of the manufacturing process, and the same surface after depositing a layer of coating graphite.

The nominal values of the process parameters were the laser power of 275 W and the scanning speed of 700 mm/s. A buried region was manufactured increasing the energy input by reducing the scanning speed down to 300 mm/s. (275 W; 300 mm/s). In this way, a deviation from the optimum process parameters occurred in a certain region of the specimen. The nominal shape and 3D dimensions of the investigated defect are indicated in figure 2 and in table 1. In particular, the analysis was focused on the upper left part indicated as the quadrant IV in figure 2.

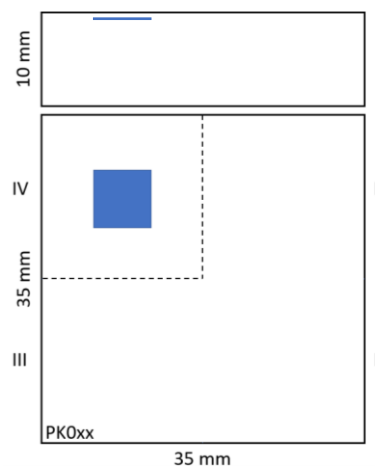


Figure 2. A simple sketch of the investigated sample. Process parameters were modified within the indicated blue region.

Table 1. Nominal process parameters and nominal geometric dimensions of the inspected specimen.

Sample identification	Scanning laser speed [mm/s]	Scanning laser power [W]	Hatch distance [mm]	Height of a single layer [μm]	Nominal depth [mm]	Nominal defect height [mm]	Nominal size IV [mm^2]
PK007	300	275	0.12	50	0.4	1 (20 layers)	6*6

2.2. Experimental μ CT campaign

Micro Computed tomography (μ CT) measurements were carried out on custom-made μ CT-Scanner using a Nikon X-ray tube XT 225 with rotating target and a Perkin-Ellmer 4k flat panel detector as depicted in figure 3. A voltage of 210 kV and a current of 550 μ A in combination with a silver pre-filter of 0.75 mm thickness was used. The flat panel detector was binned to 2k for the data acquisition. An image capturing time of 2 s per projection and six times projection averaging was used at 1500 projection angles. A voxel size of 30.8 μ m was achieved, which allows the detection of defects larger than 60 μ m. The analysis of the data was performed using porosity modules of the commercial software VG Studio MAX version 3.3. A lower threshold limit of 8 voxels was used for pore detection.

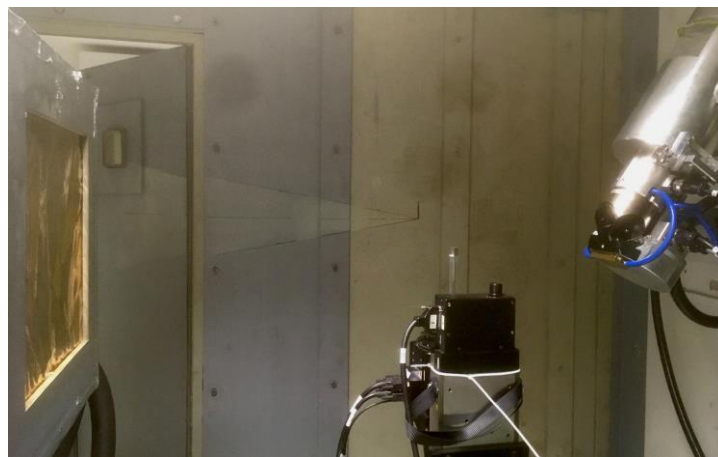


Figure 3. Experimental Setup of the custom-made Nikon-CT scanner (from left to right: detector, sample on the manipulator stage, X-ray tube).

2.3. Experimental thermographic campaign

A picture of the experimental set-up is shown in figure 4. The experiments were performed in reflection configuration, i.e. the excitation source and the infrared cooled detector were positioned at the same side of the sample. A diode laser system LDM (500-20 by Laserline GmbH), emitting at 942 nm, was used to heat the samples at one surface, widened to a top hat spatial profile of 39 mm x 39 mm. The sample was placed at the focal distance of the laser of about 60 cm in order to have a homogeneous illumination (sample size 35 mm x 35 mm < laser spot size).

Different experimental tests were carried out changing the laser pulse duration. In this regard, the energy density provided to the sample depends on the laser power and pulse duration (rectangular pulse). Moreover, the effective adsorbed energy depends on the sample surface conditions (uncoated and coated material); all these set up specifications are reported in detail in table 2. The used IR camera was the Infratec ImageIR 8800, with a cooled detector sensitive to the middle infrared wave range (MWIR, 3-5 μ m, NETD<20 mK (30°C), full frame 640 x 512 pixels, integration time 140 μ s). The adopted frame rate was of 500 Hz in all the cases, while the geometrical resolution is specified for each experimental set-up in table 2. The duration of the experimental tests was of about 10 seconds. The distance between IR camera and sample was 110 cm.

Table 2. Main experimental set-up parameters.

Test number	Sample surface	Input laser power [W]	Laser pulse duration [ms]	Absorptivity at 942 nm	Achieved energy density [Ws/cm ²]	Geometrical resolution [mm/pixel]
Test 1	uncoated	535	980	64%	22.0	0.15
Test 2	coated (graphite)	535	56	87%	1.70	0.11

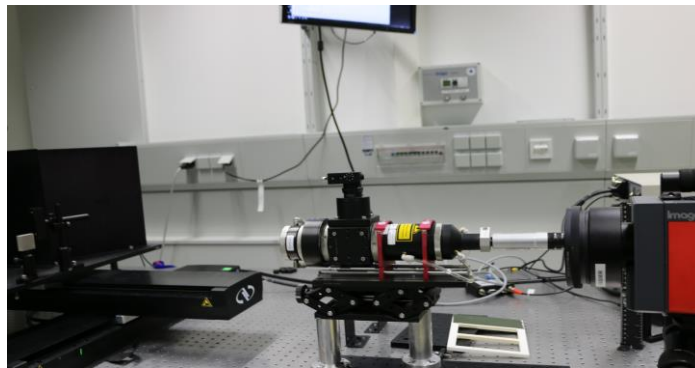
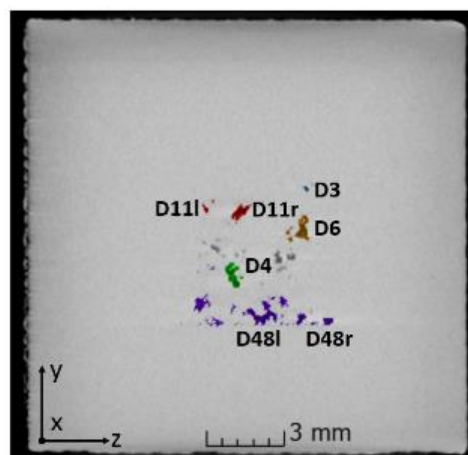


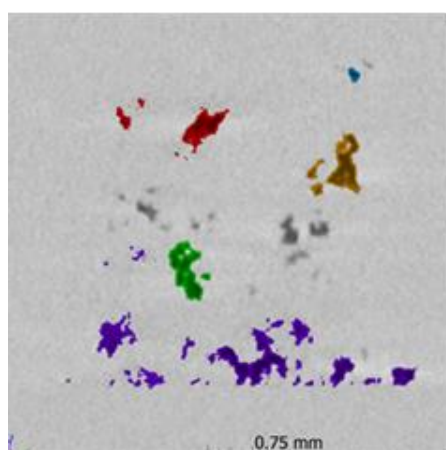
Figure 4. Thermographic set-up: thermal source widened laser beam, optic for 39x39 mm², and the IR camera Infratec ImageIR 8300 hp.

3. Experimental computed tomography results

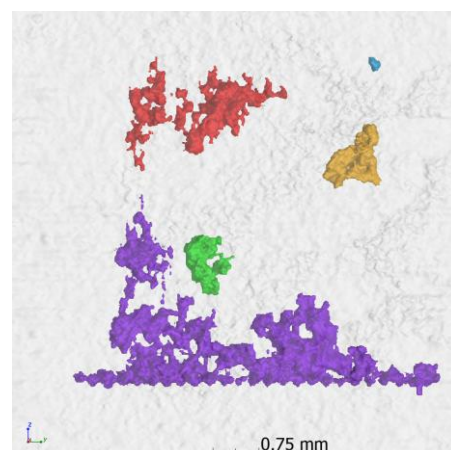
The porosity analysis of the specimen with Computed Tomography (CT) revealed the presence of different pores or microdefects consisting of small sharp-edged hollows with a complicated, almost fractal, inner surface. These segmented voids are shown in figure 5, together with a color-code used for the comparison with the experimental PT thermography and the FEM Comsol simulations. Please note the appearance of separated parts of the same defect in the shown slice (D11l and D11r as well as D48l and D48r) due to the complex structure. Figure 5c and 5e demonstrate how the apparently separated parts are connected together.



(a)



(b)



(c)

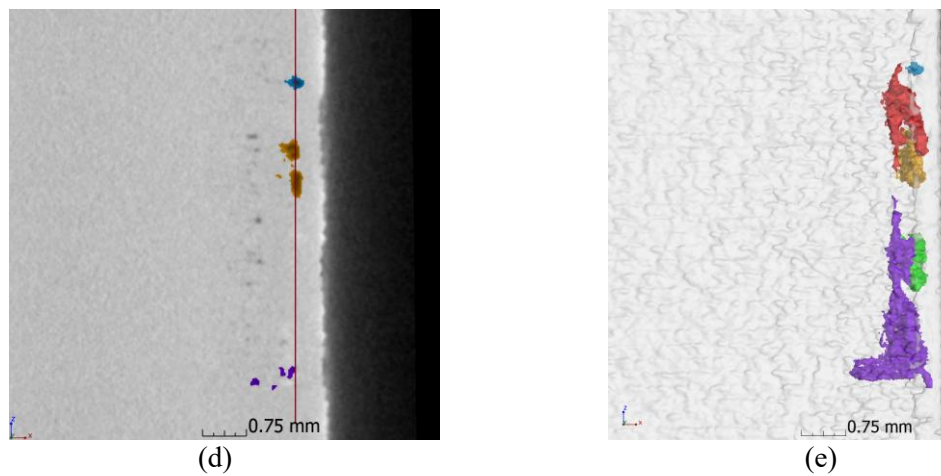


Figure 5. Results from μ CT analysis. Only five defects were selected for further analysis and they are displayed with their segmented volume; color code: D3 = light blue, D4 = green, D6 = orange, D11 = red, D48 = purple; (a) Slice of the μ CT volume taken 0.5 mm below the top surface, entire IV quadrant (five selected segmented defects are color-coded with also the used numeration), (b) Slice of the μ CT volume taken 0.5 mm below the top surface (five selected segmented defects are color-coded), (c) Front view of the 3D rendering of the five selected defects, (d) Side view slice of the μ CT volume [the red line indicates the depth position of image a)], (e) Side view of the 3D rendering of the selected defects.

4. Model for FEM simulations of the temperature distributions at the heated surface

In order to understand opportunities as well as limitations of the thermographic inspection of pores below the surface of the investigated material some FEM considerations were carried out. Since the real defect geometry is complicate with a very rugged surface as observed by the μ CT measurements only idealized simple geometries were included in the model. The following table (table 3) gives an overview about the six considered defect geometries. Please note that “splatter at surface” is not a real defect but should represent a small splatter on a surface coating.

Table 3. Drawings of the simplified defect geometries for simulations.

<p>D3</p>	<p>D6</p>	<p>splatter at surface</p>
<p>D11</p>	<p>D48</p>	<p>D4</p>

Within the model the defects were filled with air, the splatter consists of any kind of plastics. The geometrical arrangement of these models within the specimen is shown in the following Figure 6.

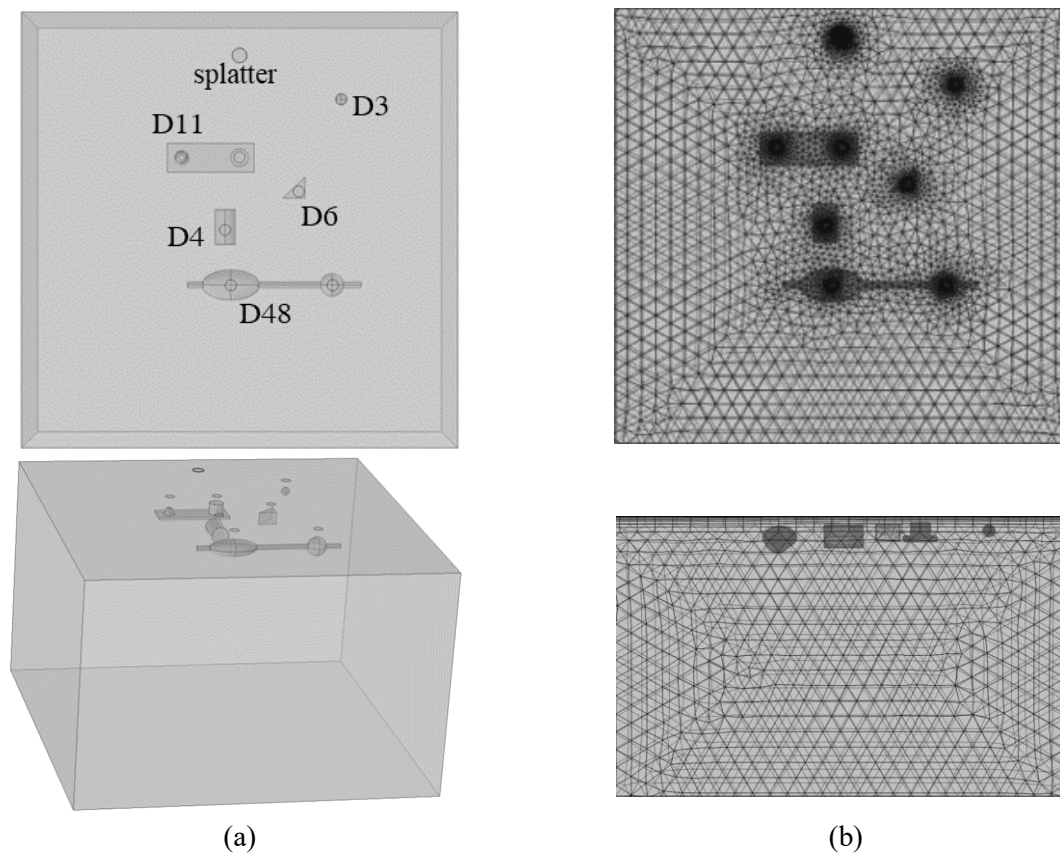


Figure 6. Model used for FEM simulations; (a) drawing of the simplified model for four inner defects and one particle as coating inhomogeneity at the surface, (b) drawing of the mesh with included defects for FEM simulations.

The heating by means of the laser pulse was implemented as a boundary source layer. The surface within the FEM was assumed to be uncoated because information about layer thickness and thermophysical properties of the coating are not available. The case of the coated specimen was described only by changed emissivity and the presence of the splatter. The next table compiles all significant parameters of the used model:

Table 4. Parameter values used for the simulation of temperature distributions.

State of surface	Laser Power density [W/cm ²]	Pulse length [ms]	Thermal conductivity [W/(m*K)]	Mass density [g/cm ³]	Heat capacity [J/(kg*K)]	Heat transfer coefficient [W/(m ² *K)]	Emissivity of front surface /
uncoated	22.5	980	14.2	7.91	500	5	0.33
coated	30.6	56	14.2	7.91	500	5	0.9

The laser power densities were corrected by the reflectivity of the respective surface at the wavelength of the laser (see table 2). Thus, in case of the uncoated surface the real power input is reduced. The material properties for the metal were deduced from other measurements not reported here. Please note that thermal conductivity and density is slightly reduced in comparison to the usual AISI 316 steel [1]. The heat transfer coefficient describes heat losses due to convection meanwhile the emissivity values were used to describe radiative heat losses. The mesh has variable element sizes and includes additional layers below the heated surface and around the included defects (see figure 6). It contains about 500,000 elements. The transients of surface temperatures above the different defects were averaged in a circular region of interest with 0.4 mm diameter and extracted for further

evaluations. Thus, they display not the maximum temperature, but a typical value measured within a small region of interest. A complete run with 56-time steps required 34 min on a Linux workstation.

5. Results and discussion

5.1. Uncoated sample: Comsol simulations and thermographic results

The general comparison between experimental and simulated results for the experiment without coating is reported in figure 7. First of all, the temperature transient in a region without defect has to be regarded. Figure 7 contains two raw data sets (blue symbols) recorded at different parts of the surface. Raw data means that no emissivity correction was carried out and the emissivity was assumed to be 1. Remarkable differences were obtained but the general curve shape is similar. The strong influence of the emissivity correction is demonstrated by the black and the cyan colored curves representing emissivity values of 33% and 40% with a background temperature of 239.9 K. Finally, the transient simulated with the COMSOL model was added to the diagram. It has to be established that the entire experimental transient cannot be simulated well, whether the rising part or the decreasing part can be simulated but not both together. At this moment we have no good explanation for this behavior, and we are investigating the phenomenon. For further considerations we focused on the decreasing part because it is more suited to detect defect related contrasts. But one has to have in mind that the simulation results help to understand the general behavior of the cooling down but cannot describe the entire experiment exactly.

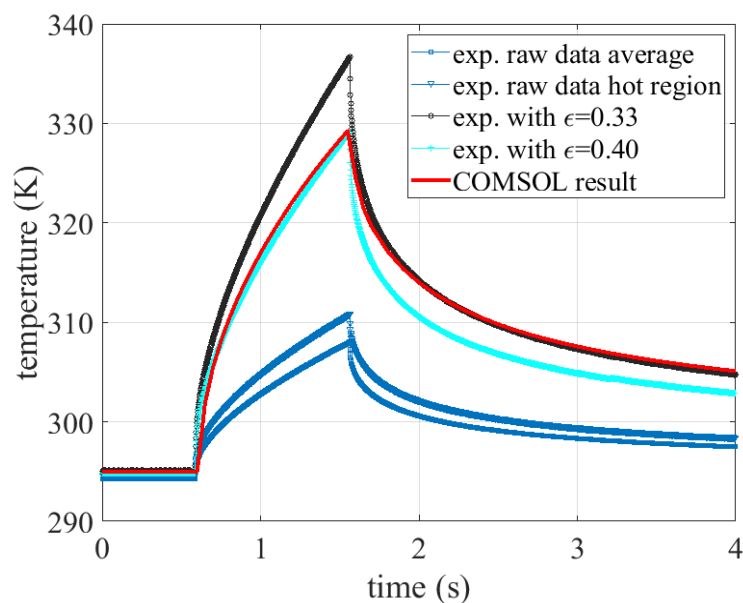


Figure 7. Comparison of experimental and simulated temperature transients for the uncoated surface in a sound region.

Figure 8 presents the simulated transients of the thermal contrast in surface regions where hidden defects are present below. Only two defects were selected here: one large (D6) and the smallest one (D3). The plot contains also transients of a coated surface to be considered later. The curves demonstrate that even the small defect D3 should be detectable during and immediately after the laser heating until the contrast drops below 100 mK after 100 ms. 100 mK is a guess for a sufficient thermal contrast in a PT experiment, actual values of the experiments are shown in table 6. The larger defects should be detectable even 1 s after the end of the laser heating. Both curves allow the conclusion that very short pulses of 200 ms or shorter should be sufficient to generate measurable thermal contrasts above these defects situated below, but near the surface.

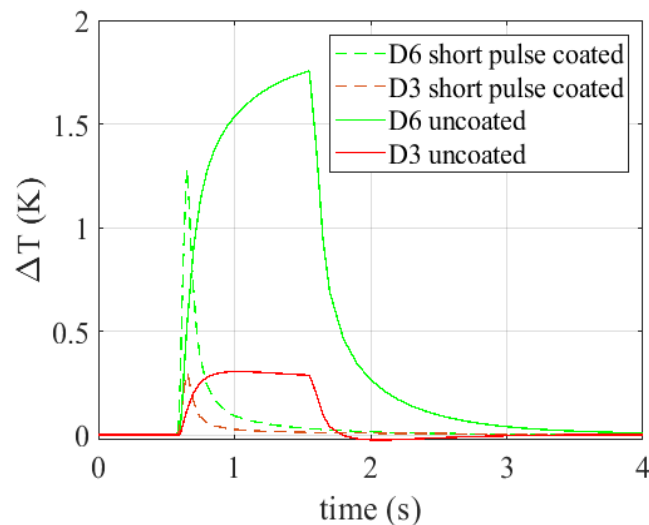


Figure 8. Simulated temperature contrasts at the defects D6 and D3 for the uncoated case (long pulse) and the coated case (short pulse).

However, an infrared camera can only detect those contrasts if the surface has a very high emissivity near 1. In case of metallic surface, the emissivity is certainly reduced, and the camera records a signal which includes a partial reflection of the temperature of the surrounding. This is demonstrated in figure 9, where figure 9a) presents the simulated real temperature distribution 100 ms after the pulse (980 ms long). Regarding the guessed emissivity of 0.33 an infrared camera might detect the apparent temperature distribution shown in figure 9b). Regarding a spatial emissivity distribution deduced from the first thermograms before the heating, the result in a thermogram as shown in figure 9c) is obtained. Here, the grainy spatial pattern of emissivity variations covers the defect related thermal contrasts completely.

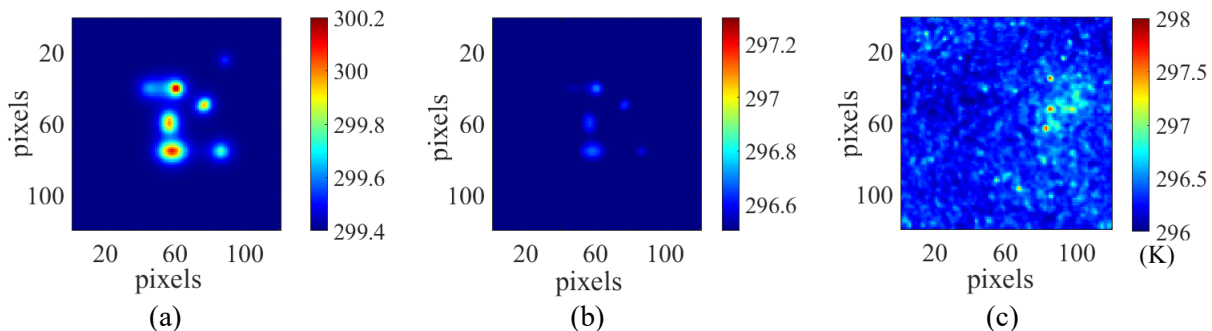


Figure 9. (a) Simulated temperature distribution 100 ms after the heating pulse; (b) simulated apparent temperature distribution 100 ms after the heating pulse regarding a homogeneous emissivity of 0.33 and a background temperature of 293.9 K; (c) simulated apparent temperature distribution 100 ms after the heating pulse regarding an inhomogeneous emissivity distribution and a background temperature of 293.9 K.

Thus, the simulations results predict that it will not be possible to detect the pores by means of simple temperature contrast evaluation.

The experimental results confirm this prediction. Figure 10 displays two thermograms with the same temperature scale recorded directly after the heating most suited for the detection of very shallow defects.

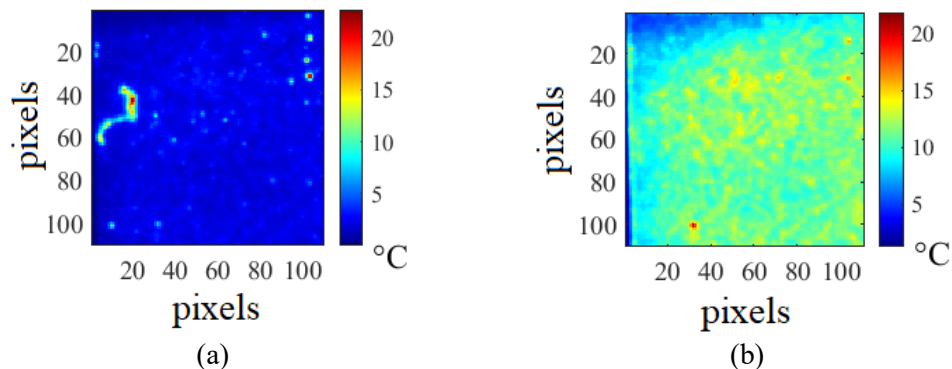


Figure 10. Thermograms related to the uncoated experimental test (Test 1); (a) thermogram recorded 30 ms after the heating pulse; (b) thermogram recorded 100 ms after the heating pulse.

However, the application of further data evaluations focusing on the temporal behavior of thermal contrasts enable the detection of some defects as shown later.

5.2 Coated sample: Consol simulations and thermographic results

The application of a coating should suppress the emissivity inhomogeneities showed above and force the energy input by means of electromagnetic irradiation. The question is, if a subsequent coating enables a better detectability for the hidden micropores. Additionally, a splatter was included in the simulation to model the influence of a localized irregularity which can occur within the coating.

Figure 11a contains the simulated transient of two defect (D6 and D3) related contrasts of a black-coated surface in the short-pulse heating modus (parameters are given in table 4). Here, the pulse length was shortened down to 56 ms. Please note the faster contrast increase during the pulse because of the enhanced introduced laser power density.

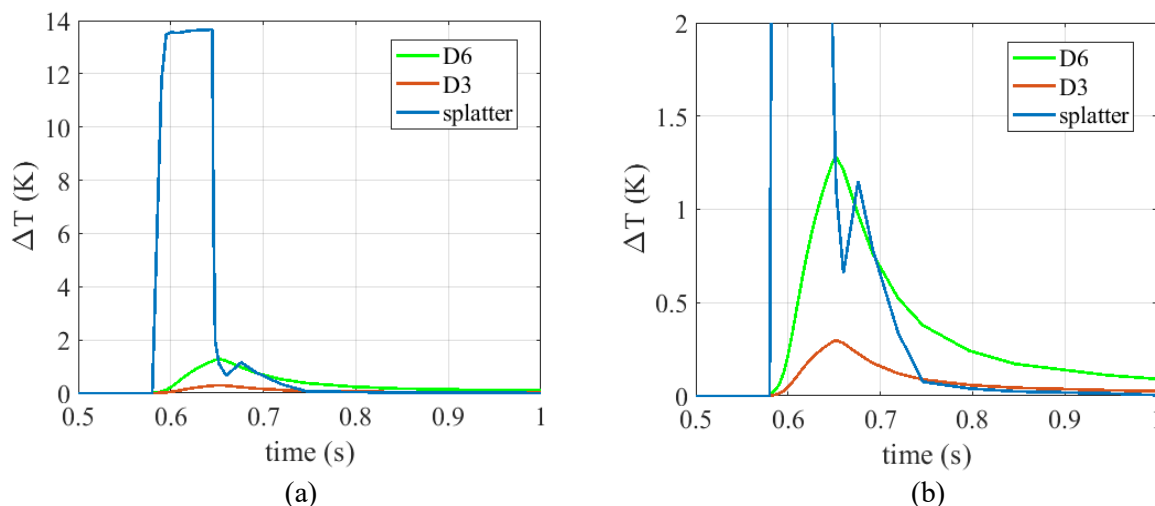


Figure 11. (a) Comparison of the simulated contrast transients during and after the pulse heating for two defects and the splatter and (b) enlarged part of the same.

The influence of the splatter (figure 11) can be studied showing the contrast transients of D6 and D3 in comparison to a contrast which arises at the splatter. The contrast at the splatter is high in comparison to defect related contrasts but disappears quickly in comparison to the contrast at D6. On the other side, it could map small defects like D3 with fast contrast drop. However, this is only a rough simulation to demonstrate the behavior of such splatters in principle. The spike at the dropping part of the splatter transient indicates that the FEM simulation reached its limit at this extreme geometry where a 25 μm thin disc is considered at a 1 cm thick specimen in millisecond time resolution.

The related experimental results are demonstrated in figure 12. Here, 3 thermograms recorded after the heating period are given. The first one is directly after the end of the heating pulse (figure 12a). The dynamic range of the thermogram is determined by 3 hot spots in the upper half associated with splatters. The regions of the defects cannot be distinguished from the sound, only the largest D11 right and D8 left are detectable.

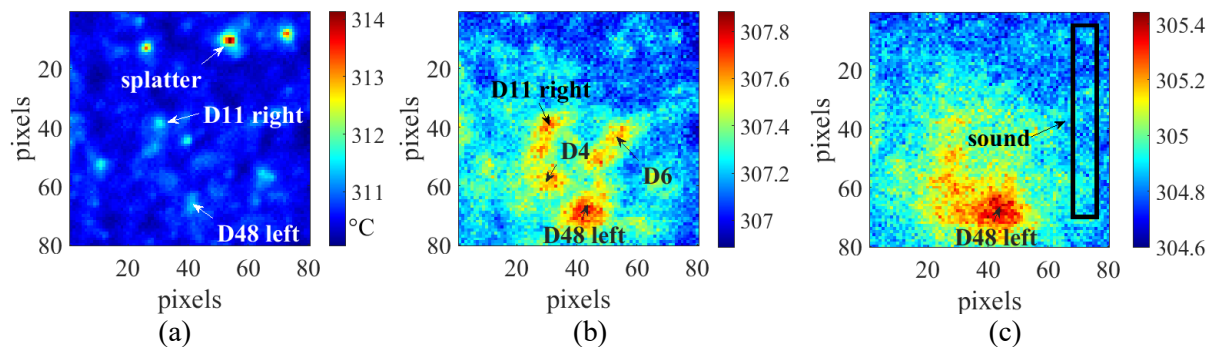


Figure 12. Thermograms related to the coated experimental test (Test 2); (a) thermogram directly after the heating pulse, (b) thermogram 20 ms after the heating pulse, (c) thermogram 100 ms after the heating pulse, crop coordinates x 40:119, coordinates y 45:124 respect to an entire thermogram/map.

The thermogram in figure 12b was recorded 20 ms after the pulse and reveals striking thermal contrasts within the regions with the subsurface defects. The splatters are also still visible but weakened. The last thermogram (figure 12c) obtained after 100 ms shows that detectable thermal contrasts are available, but their shape is blurred, and smaller defects cannot be separated from each other.

The following figure 13 provides the transient corresponding to the simulation results shown before.

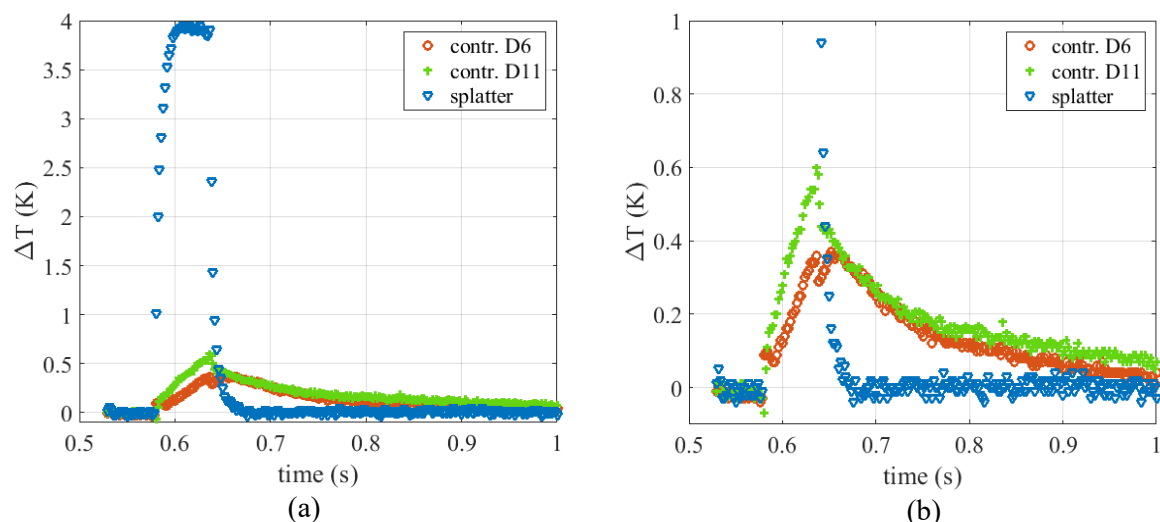


Figure 13. (a) Comparison of the measured contrast transients during and after the pulse heating for two defects and the splatter and (b) enlarged part of the same.

The general relation between splatter and defect related contrasts is very similar to the simulation, the splatter causes a very high thermal contrast which is disappearing very quickly after the end of the heating pulse. Please note also the differences between simulation (figure 11) and experiment (figure 13): the simulation predicts larger contrasts for both D6 as well as the splatter. This is probably due to the simplifications of the geometries within the model. In particular, in case of D6 we have an overestimation for the simulation by factor 3 (compare figure 11b and 13b). The obtained reducing

factor 3 can be interpreted as a form factor to correct the shape simplifications of the model and has to be regarded if direct comparisons of experimental data with the simulation results are carried out.

5.3 Pulsed Phase Thermography (PPT) at the uncoated sample

A common post-processing algorithm of analysis, i.e. Pulsed Phase Thermography [18], [20]-[22] was applied to the raw thermal data, considering different frequencies of analysis and so different truncation window sizes for the post processing of the acquired thermographic sequence. Three different results in terms of phase maps related to three different frequencies of analysis are reported in figure 14, considering 2 different truncation window sizes, 4 seconds of analysis for the result in figure 14a, and 2 seconds of analysis for the phase maps in figure 14b and figure 14c. These results show clearly the presence of different voids found with the μ CT, if a higher frequency of analysis is analysed (figure 14b and c), related, obviously, to a shallow depth. Moreover, it is important to highlight as the PPT algorithm allows for increasing the signal to noise ratio, acting as an analysis filter, and then detecting defects, although the emissivity surface variations are present. However, as already explained, due to the low emissivity values, it is necessary to use a high laser power density to detect defects without the coating. As it is shown in table 2, the maximum laser power of the setup and a pulse duration of 980 ms were used for obtaining the suitable laser power density. In particular, the high laser pulse duration allows for increasing the thermal contrast but reducing the capability of discerning contiguous defects due to the increase of heat diffusion effects.

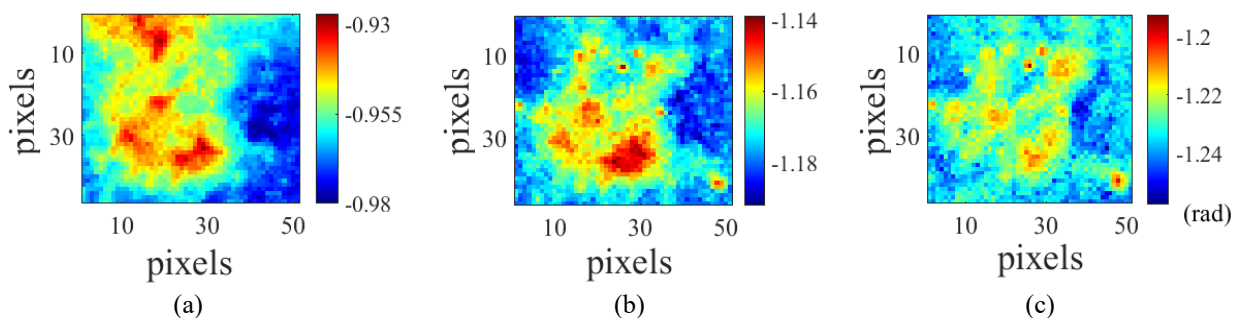


Figure 14. PPT algorithm (cooling down, long pulse analysis). Phase maps (a) 0.24 Hz, (b) 0.98 Hz, (c) 1.46 Hz; Test 1, crop coordinates x 50:95 pixels, coordinates y 55:100 pixels respect to an entire thermogram/map.

6. Comparing μ CT and experimental PT results

To compare these results with those from the experiments with coating, for each pixel of the obtained phase maps, the normalized contrast is calculated by subtracting from the thermal signal the mean of the sound signal and dividing by the related standard deviation; as reference signal the sound area indicated in figure 12c was chosen. In figure 15, the results obtained for the frequency of 0.98 Hz is shown (0.98 Hz) as example of the obtained results with this operation.

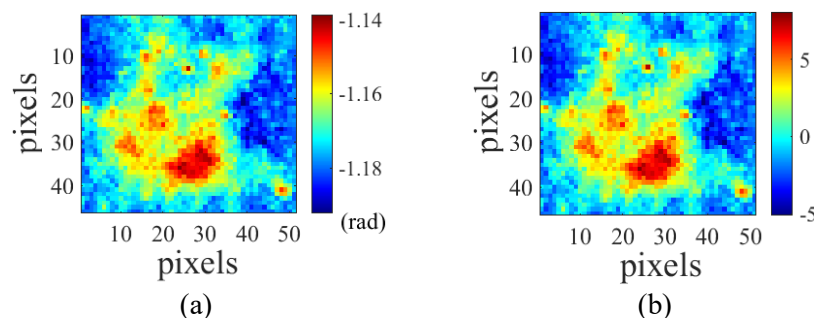


Figure 15. (a) Phase map related to the frequency of 0.98 Hz (cooling down, 2 seconds of analysis, and (b) related normalized phase contrast map; uncoated sample Test 1.

In figure 16 and 17, a direct final comparison is shown between the final results obtained with the 2 different techniques μ CT and PT. Figure 16 is a scheme that shows the entire quadrant with the indication of the investigated defects with the reference system for both techniques. The same maps are also shown in figure 17 and they are magnified to show the defects as large as possible. For the thermographic result is also indicated the position in millimetres, using the geometrical resolution calculated in the experimental tests (0.15 mm/pixel Test 1 and 0.11 mm/pixel, Test 2).

In table 5, the coordinates for each defect are shown, obtained from the μ CT results. It is necessary to underline that for μ CT analyses the used commercial software contains a module for the automatic registration of pores, which have usually a spherical shape. Thus, in this case, the diameter is indeed a kind of equivalent diameter, that can be considered as a typical dimension. In case of D48, in fact, it represents the defect length and not the diameter. μ CT results allow for obtaining information about the shape and defect 3D dimensions. The dimensions of the defects on the y-z plane (table 5) will be used as a reference for the discussion of the obtained thermographic results.

For the thermographic results, the y-z coordinates are reported in table 6. Here, normalized results of both thermographic tests are listed together including the analysis frequency and the selected time. In this regard, it is necessary to underline that the small differences in the last column of table 6 are due to the noise of the measure.

In both cases, the application of a Gaussian filter was deemed necessary, following the previous described operations to obtain the normalized contrast (standard deviation 0.85).

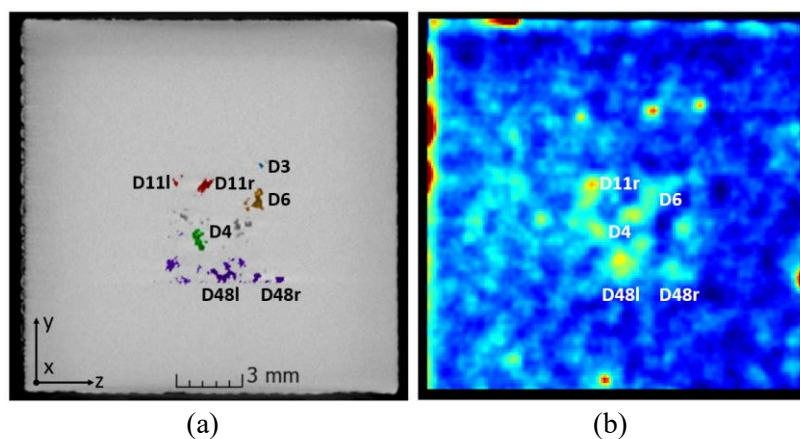


Figure 16. Direct comparison between μ CT and PT results, entire quadrant IV; (a) slice of the μ CT volume taken 0.5 mm below the top surface and (b) PT result at 0.066 s (map chosen as an example of the obtained PT results) with the indication of the chosen defects for the discussion.

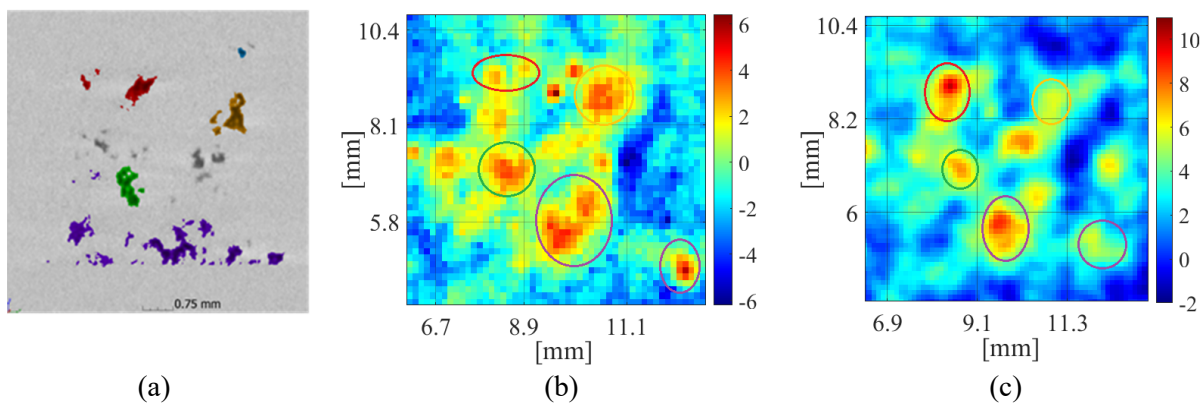


Figure 17. Direct comparison between μ CT and PT results, zoom to the exact defects position; (a) slice of the μ CT volume taken 0.5 mm below the top surface and (b) PT result at 0.066 s related to the Test 2 conditions.

Table 5. μ CT results x, y and z coordinates for each investigated defect.

Pore number	x [mm]	y [mm]	z [mm]	Diameter [mm]	Volume [mm ³]	Surface [mm ²]
48	8.34	8.69	5.59	6.19	1.37	53.54
11	8.5	7.86	9.2	2.83	0.29	12.02
6	8.81	10.29	8.61	1.29	0.12	4.10
4	8.77	7.93	6.84	1.09	0.11	3.58
3	8.81	10.61	10.13	0.35	0.01	0.29

Table 6. PT experimental results. Values of the normalized phase contrast (Test 1) and the normalized thermal contrast (Test 2) with an indication of the position in the frequency and time axis and y, z position with the same coordinate system of μ CT results.

Pore number	y [mm]	z [mm]	Normalized phase contrast	Position in the frequency axis [Hz]	Normalized contrast	Position in the time axis [s]
48	9.03	5.68	4.98	1.46	7.66	0.066
11	8.03	9.02	3.22	1.46	8.16	0.070
6	10.67	8.8	3.57	1.46	5.53	0.068
4	8.17	7.04	3.88	1.46	6.41	0.071
3	/	/	/	/	/	/

From the direct comparison of the results obtained, it is possible to note that the defect indicated as D3 represents the limits of the thermographic technique among the investigated defects, with an equivalent diameter of about 0.35 mm, a depth of about 0.4 mm and a simulated theoretical maximum contrast equal to 0.3 K, below the signal to noise ratio reached in both experimental tests (if we consider 2 or 3 times the standard deviation value, obviously). To understand better this crucial point, table 7 summarises the experimental results in this sense, reporting the value of the standard deviation (in all the cases for the area indicated in figure 12c, 350 pixels). The reported values were determined at the previously presented spatial temperature and considering the phase angle distributions; in particular, we are referring to: Test 1 temperature – figure 10 a and b; Test 1 phase angle – figure 14 c; Test 2 temperature – figure 12 a, b and c (20 ms ~ time related to the maximum contrast).

It should be also underlined that the real reason for the differences among the simulated and the experimental contrasts is due to the rough simulation model of the defects. Neglecting the filigree structure of the defects the deduced thermal contrasts are obviously overestimated as noted before. In case of D6 we have an overestimation by factor 3 (compare figure 11b and 13b).

Table 7. PT experimental results. Values related to the sound standard deviation considering the main results related to both experimental tests.

Time [s]	Test 1, uncoated material		Test 2, coated material	
	Sound standard deviation (temperature)	Frequency [Hz]	Sound standard deviation (phase of PPT)	Sound standard deviation (temperature)
0.030 heating	0.67	1.46	0.0048	0.056
0.100 cooling	0.73			0.076
				0.156
				0.068

Finally, the defect indicated as D48 right appears as a separated defect in the slice of the μ CT volume taken 0.5 mm below the top surface (figure 5). PT can detect this sub defect only very shortly

after the heating (figure 12). Similar considerations can be made for the defects D6 and D11, stressing again the fast speed of the thermal phenomenon investigated. Obviously, this is related to diffusive blurring of contrasts reducing the spatial resolution.

7. Conclusions

To understand, to demonstrate and to explain the opportunities and the limits of the pulsed technique in terms of detectability and localizability of AM keyhole pores, a combined analysis with a double experimental and theoretical (COMSOL simulations) approach was assessed by comparing the active thermographic approach with μ CT investigations, obtaining results that show a good agreement between the two techniques.

In particular, μ CT results demonstrate the presence of a network of voids (microdefects consisting of small sharp-edged hollows with a complicated, almost fractal, inner surface), especially in the first layers below the investigated surface. A similar result was obtained by applying the thermographic technique, investigating the first instants of time of the cool down period, and higher frequencies (0.98 Hz-1.46 Hz) related to short observation periods when applying the PPT algorithm corresponding to lower depths.

The surface was investigated by pulsed thermographic technique with and without coating.

The following conclusive considerations emerge from the combined experimental-simulated analysis:

- ✓ both Exp-PT and FEM results explain clearly why no indication of defect related to the thermal contrasts could be found during the investigation of an uncoated surface. However, the application of further data evaluations focusing on the thermal behavior and emissivity evaluation (PPT post data processing) enable the detection of some defects;
- ✓ coating facilitates a closer inspection of inner defects, but inhomogeneities of the coating could impair the spatial resolution and lead to the emergence of hotspots (the FEM simulation reached its limit with this extreme geometry where a 25 μ m thin disc is considered at a 1 cm thick specimen in millisecond time resolution);
- ✓ both Exp-PT and FEM results allow the conclusion that very short pulses of 200 ms or shorter should be sufficient to detect these defects below, but near the surface;
- ✓ a short duration of the thermal phenomenon should be emphasized, about 0.04 s (high frame rate camera);
- ✓ in the case of the uncoated material, a pulse duration of 1000 ms was used to achieve the necessary power density; please note that the power density of solar irradiation is about 0.1 W/cm² and that with an usual halogen lamp heating only 0.025 W/cm² [28] can be achieved. Thus, the application of a powerful laser with beam expansion is strongly recommended for the detection of small microdefects in this material class;
- ✓ Exp-PT results allow the detection and localization of these different pores, in accordance with the μ CT results; however, among the available and investigated defects, the defect D3 represents the detection limit of the PT technique (size 0.35 mm and depth ~0.4 mm).

Further investigations can be summarized as follows:

- FEM simulations with different PT test parameters and typical AM defect geometries and properties to assess and investigate the opportunities and the limits of the technique and to find the optimum test conditions for each case study;
- handling of the problem with the simulation of the entire temperature transient during a PT experiment;
- Exp-PT investigation using a higher-speed camera, and also an assessment in terms of pulse duration and energy density, by applying also other heating source;
- assessment in terms of material thermophysical properties for a thermal depth estimation of pores.

Author Contributions: conceptualization and methodology: Ester D'Accardi, Rainer Krankenhagen, Davide Palumbo and Umberto Galietti; resources and design of samples and experiments: Simon Altenburg, Christiane Maierhofer, Gunther Mohr, Kai Hilgenberg; writing-original draft preparation: Ester D'Accardi; draft review: Rainer Krankenhagen and Davide Palumbo; Comsol simulations: Rainer Krankenhagen; μ CT experimental tests and results: Alexander Ulbricht; PT experimental tests: Ester D'Accardi.

Acknowledgments: The samples used for these experiments are provided within the BAM project ProMoAM thanks for cooperation of Gunther Mohr and Kai Hilgenberg. The authors would like to thank also Dietmar Meinel, who started some of the μ CT measurements when there was restricted access to the labs for Covid situation.

Conflicts of Interest: the authors declare no conflict of interest.

References

- [1] DebRoy, T., Wei, H. L., Zuback, J. S., Mukherjee, T., Elmer, J. W., Milewski, J. O., ... & Zhang, W. 2018. Additive manufacturing of metallic components—process, structure and properties. *Progress in Materials Science*, **92**, 112-224.
- [2] ASTM Committee F42 on Additive Manufacturing Technologies, & ASTM Committee F42 on Additive Manufacturing Technologies. Subcommittee F42. 91 on Terminology. 2012. Standard terminology for additive manufacturing technologies. ASTM International.
- [3] Mani, M., Feng, S., Lane, B., Donmez, A., Moylan, S., & Feserman, R. 2015. Measurement science needs for real-time control of additive manufacturing powder bed fusion processes.
- [4] Vlasea, M. L., Lane, B., Lopez, F., Mekhontsev, S., & Donmez, A. 2015, August. Development of powder bed fusion additive manufacturing test bed for enhanced real-time process control. In *Proceedings of the International Solid Freeform Fabrication Symposium*, Austin, TX, USA (pp. 13-15).
- [5] Mohr, G., Altenburg, S. J., Ulbricht, A., Heinrich, P., Baum, D., Maierhofer, C., & Hilgenberg, K. 2020. In-Situ Defect Detection in Laser Powder Bed Fusion by Using Thermography and Optical Tomography—Comparison to Computed Tomography. *Metals*, **10**(1), 103.
- [6] King, W. E., Barth, H. D., Castillo, V. M., Gallegos, G. F., Gibbs, J. W., Hahn, D. E., ... & Rubenchik, A. M. 2014. Observation of keyhole-mode laser melting in laser powder-bed fusion additive manufacturing. *Journal of Materials Processing Technology*, **214**(12), 2915-2925.
- [7] Coeck, S., Bisht, M., Plas, J., & Verbist, F. 2019. Prediction of lack of fusion porosity in selective laser melting based on melt pool monitoring data. *Additive Manufacturing*, **25**, 347-356.
- [8] Thanki, A., Goossens, L., Mertens, R., Probst, G., Dewulf, W., Witvrouw, A., & Yang, S. 2019. Study of keyhole-porosities in selective laser melting using X-ray computed tomography. *Proceedings of iCT 2019*, 1-7.
- [9] Slotwinski, J. A., Garboczi, E. J., & Hebenstreit, K. M. 2014. Porosity measurements and analysis for metal additive manufacturing process control. *Journal of research of the National Institute of Standards and Technology*, **119**, 494.
- [10] Shin, H. S., Kim, K. Y., & Pande, G. N. 2013. Porosity and pore-size distribution of geomaterials from X-ray CT scans. In *Multiphysical testing of soils and shales* (pp. 177-186). Springer, Berlin, Heidelberg.
- [11] Elmer, J. W., Vaja, J., Carlton, H. D., & Pong, R. 2015. The effect of Ar and N₂ shielding gas on laser weld porosity in steel, stainless steels, and nickel. *Weld J*, **94**(10), 313s-325s.
- [12] Elmer, J. W., Vaja, J., & Carlton, H. D. 2016. The effect of reduced pressure on laser keyhole weld porosity and weld geometry in commercially pure titanium and nickel. *Welding Journal*, **95**(11), 419S-430S.

- [13] Girardin, E., Renghini, C., Dyson, J., Calbucci, V., Moroncini, F., & Albertini, G. 2011. Characterization of porosity in a laser sintered MMCp using X-ray synchrotron phase contrast microtomography. *Materials Sciences and Applications*, **2**(9), 1322-1330.
- [14] Aboulkhair, N. T., Everitt, N. M., Ashcroft, I., & Tuck, C. 2014. Reducing porosity in AlSi10Mg parts processed by selective laser melting. *Additive Manufacturing*, **1**, 77-86.
- [15] Altenburg, S. J., Maierhofer, C., & Gumenyuk, A. 2018. Comparison of MWIR thermography and high-speed NIR thermography in a laser metal deposition (LMD) process.
- [16] D'Accardi, E., Altenburg, S., Maierhofer, C., Palumbo, D., & Galietti, U. 2019. Detection of Typical Metal Additive Manufacturing Defects by the Application of Thermographic Techniques. In *Multidisciplinary Digital Publishing Institute Proceedings* (Vol. **27**, No. 1, p. 24).
- [17] Tomić, L. D., et al. Application of Pulsed Flash Thermography Method for Specific Defect Estimation 2015, in *Aluminum, Thermal Science*, **19**, 5, pp. 1845-1854.
- [18] Ibarra-Castaneda, C., & Maldague, X. P. 2004, April. Defect depth retrieval from pulsed phase thermographic data on plexiglas and aluminum samples. In *Thermosense XXVI* (Vol. **5405**, pp. 348-357). International Society for Optics and Photonics.
- [19] Ranjit, S., & Kim, W. T. (2014). Detection of Subsurface Defects in Metal Materials Using Infrared Thermography: Image Processing and Finite Element Modeling. *비파괴검사학회지*, **34**(2), 128-134.
- [20] Müller, J. P., Dell'Avvocato, G., & Krankenhagen, R. 2020. Assessing overload-induced delaminations in glass fiber reinforced polymers by its geometry and thermal resistance. *NDT & E International*, 102309.
- [21] D'Accardi, E., Palumbo, D., Tamborrino, R., & Galietti, U. 2018. A quantitative comparison among different algorithms for defects detection on aluminum with the pulsed thermography technique. *Metals*, **8**(10), 859.
- [22] D'Accardi, E., Palano, F., Tamborrino, R., Palumbo, D., Tati, A., Terzi, R., & Galietti, U. 2019. Pulsed phase thermography approach for the characterization of delaminations in CFRP and comparison to phased array ultrasonic testing. *Journal of Nondestructive Evaluation*, **38**(1), 20.
- [23] Hendorfer, G., Mayr, G., Zauner, G., Haslhofer, M., & Pree, R. 2007, March. Quantitative determination of porosity by active thermography. In *AIP conference proceedings* (Vol. **894**, No. 1, pp. 702-708). American Institute of Physics.
- [24] Maierhofer, C., Röllig, M., Ehrig, K., Meinel, D., & Céspedes-Gonzales, G. 2014. Validation of flash thermography using computed tomography for characterizing inhomogeneities and defects in CFRP structures. *Composites Part B: Engineering*, **64**, 175-186.
- [25] Sreedhar, U., Krishnamurthy, C. V., Balasubramaniam, K., Raghupathy, V. D., & Ravisankar, S. 2012. Automatic defect identification using thermal image analysis for online weld quality monitoring. *Journal of Materials Processing Technology*, **212**(7), 1557-1566.
- [26] Myrach, P., Jonietz, F., Meinel, D., Suwala, H., & Ziegler, M. 2017. Calibration of thermographic spot weld testing with X-ray computed tomography. *Quantitative InfraRed Thermography Journal*, **14**(1), 122-131.
- [27] Maierhofer, C., Myrach, P., Röllig, M., Jonietz, F., Illerhaus, B., Meinel, D., ... & Miksche, R. 2016, February. Characterization of pores in high pressure die cast aluminum using active thermography and computed tomography. In *AIP Conference Proceedings* (Vol. **1706**, No. 1, p. 110009). AIP Publishing LLC.
- [28] Müller, J. P., & Krankenhagen, R. 2019. Optimizing thermographic testing of thick GFRP plates by assessing the real energy absorbed within the material. *Composite Structures*, **215**, 60-68.